JACS Au
AN OPEN ACCESS JOURNAL OF THE AMERICAN CHEMICAL SOCIETY

pubs.acs.org/jacsau
Article

A BODIPY-Naphtholimine-BF_2 Dyad for Precision Photodynamic Therapy, Targeting, and Dual Imaging of Endoplasmic Reticulum and Lipid Droplets in Cancer

Nitish Chauhan,[‡] Mrunesh Koli,[‡] Rajib Ghosh, Ananda Guha Majumdar, Ayan Ghosh, Tapan K. Ghanty, Soumyaditya Mula,* and Birija Sankar Patro*

Cite This: *JACS Au* 2024, 4, 2838−2852
Read Online

ACCESS | Metrics & More | Article Recommendations | Supporting Information

ABSTRACT: Currently, effective therapeutic modalities for pancreatic ductal adenocarcinoma (PDAC) are quite limited, leading to gloomy prognosis and ∼6-months median patient survival. Recent advances showed the promise of photodynamic therapy (PDT) for PDAC patients. Next generation photosensitizers (PS) are based on "organelle-targeted-PDT" and provide new paradigm in the field of precision medicines to address the current challenge for treating PDAC. In this investigation, we have constructed a novel PS, named as **N*b*B**, for precise and simultaneous targeting of endoplasmic reticulum (ER) and lipid droplets (LDs) in PDAC, based on the fact that malignant PDAC cells are heavily relying on ER for hormone synthesis. Our live cell imaging and fluorescence recovery after photobleaching (FRAP) experiments revealed that **N*b*B** is quickly targeted to ER and subsequently to LDs and shows simultaneous dual fluorescence color due to polar and nonpolar milieu of ER and LDs. Interestingly, the same molecule generates triplet state and singlet oxygen efficiently and causes robust ER stress and cellular lipid peroxidation, leading to apoptosis in two different PDAC cells in the presence of light. Together, we present, for the first time, a potential next generation precision medicine for ER-LD organelle specific imaging and PDT of pancreatic cancer.

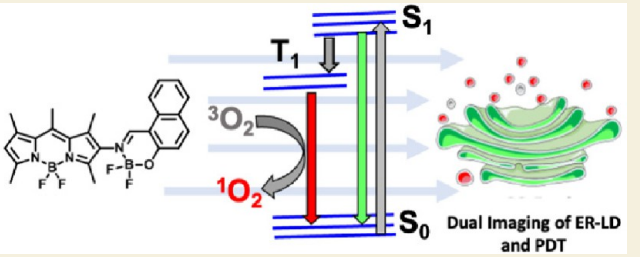

KEYWORDS: *BODIPY-naphtholimine-BF_2, PDT, Endoplasmic reticulum, Lipid droplets, ER stress, Dual imaging, Pancreatic cancer*

INTRODUCTION

Pancreatic ductal adenocarcinoma (PDAC) is one of the most difficult to treat cancers with dismal and grim prognosis rate, while treatment options are also quite limited.[1,2] Pancreatic cells are heavily involved in hormone and digestive enzyme synthesis and secretion, with an extensive network of endoplasmic reticulum (ER).[3] Besides, malignant cells rely on ER functionality for the requirement of heavy protein synthesis.[4] ER is a hub for different signaling pathways and acts as a double-edged sword at the interface of cell survival and death. ER is also involved in the generation of lipid droplets (LDs), which in turn are positively correlated with advanced clinical staging, metastasis, and poor survival.[5,6] These factors make the ER and LDs attractive targets for sensitizing malignant PDAC cells.[7] Although multiple approaches have failed, a growing number of studies have indicated that photodynamic therapy (PDT) may be a viable approach for treatment of pancreatic tumors. Especially clinical trials with PDT agents, meso-tetra(hydroxyphenyl)chlorin, and verteporfin showed some positive therapeutic outcomes for PDAC patients.[8] However, simultaneous targeting of ER and LD organelles for the PDT of PDAC is not yet fully explored. Development of such precision photomedicines may improve the outcomes of PDT, and it may also address the unmet challenge of PDAC treatment.

For targeting and imaging of ER and LD, few interesting recent reports showed (i) imaging of ER[9−11] or LD[12−16] with multiple probes and (ii) simultaneous imaging of ER and LD with one single probe but with one emission color,[17,18] leading to inherent difficulties in discriminating structure and functions of ER and LDs. To the best of our knowledge, only one elegant study on a single probe (3-hydroxyflavone system) for simultaneous imaging of ER and LDs with dual emission color was reported.[19] 3-Hydroxyflavone system, however, lacks photosensitization properties for selective killing of cancer cells. In this regard, we report for the first time a single agent with multiple functionalities: (1) high ER and LDs specific targeting, (2) simultaneous imaging of ER and LDs with dual fluorescence, and (3) photosensitization of both ER and LDs

Received: September 13, 2023
Revised: May 11, 2024
Accepted: May 22, 2024
Published: June 5, 2024

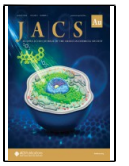

for cancer therapy (Figure 1A). We and others have shown that fluorinated boron-dipyrromethene (BODIPY)-based

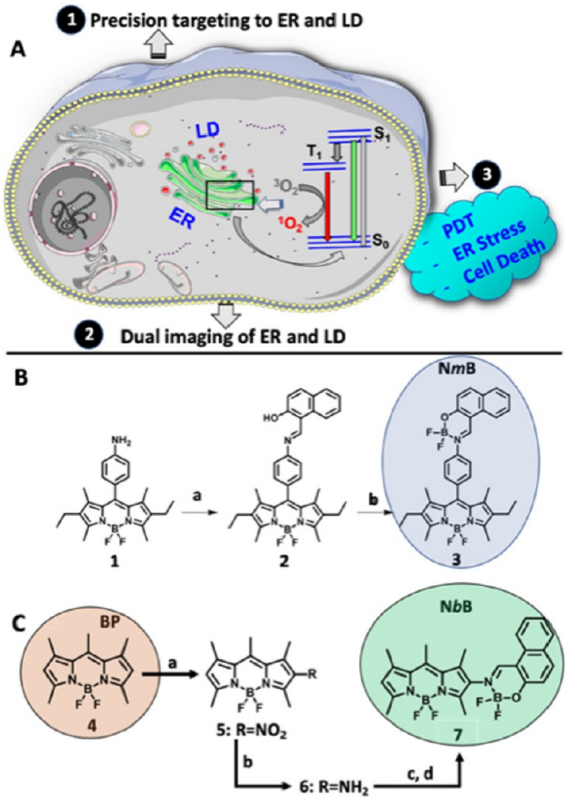

Figure 1. Targeting and synthesis of molecules for ER-LD specific PDT. (A) Potential of a single molecule for targeting, dual imaging of ER and LD and photosensitization of cancer. (B) Synthesis routes of N*m*B: (a) 2-Hydroxy-1-naphthaldehyde, dry MeOH, reflux, 4 h; (b) *i*-Pr_2NEt, $BF_3{\cdot}OEt_2$, dry DCE, 85 °C, 12 h. (C) Synthesis routes of N*b*B: (a) HNO_3, 0 °C, 90 min; (b) HCO_2NH_4, Zn, MeOH, 25 °C, 10 min; (c) 2-Hydroxy-1-napthaldehyde, dry MeoH, reflux, 4 h; (d) *i*-Pr_2NEt, $BF_3{\cdot}OEt_2$, dry DCE, 85 °C, 12 h.

systems are promising design choices individually for cellular imaging, photosensitization and targeting.[20−22] Further, for functional tuning and rational designing of an advanced PDT agent, we have chosen "Naphthalene Scaffold" for following attributes. (i) **ER targeting**: Naphthalene based various natural and synthetic drugs target ER membrane efficiently.[23−25] (ii) **Simultaneous ER-LD dual imaging**: Considering relatively more hydrated liquid disordered phase in ER membrane than LD, we anticipated that self-aggregation properties of naphthalene moiety[26,27] may influence the fluorescence emission of BODIPY backbone in ER and LDs. (iii) **Photosensitizing properties**: One of the key requirements for the PDT is generation of singlet oxygen ($^1O_2$) through energy transfer from excited triplet state (T_1) of PS to molecular oxygen. In general, BODIPYs are highly fluorescent with very low triplet quantum yields. Although BODIPY substituted with iodine/bromine are reported for efficient $^1O_2$ generation for PDT,[28,29] toxic heavy atoms are least preferred in drugs or biological studies. Lately, heavy atom free orthogonal BODIPY dimers are also considered as efficient triplet PSs. A recent preliminary study has shown *meso*-substituted BODIPY with naphthalene make them good PS, which generate T_1 and $^1O_2$ efficiently.[30] Moreover, *meso*- and *β*-substitutions have a profound effect on the excited state dynamics of the BODIPY.[28,31] However, nothing is attempted yet to explore the photophysical, photochemical and photobiological roles of such dyads, where modified napathalene is conjugated to BODIPY in the form of naphtholimine boron complex (naphtholimine-BF_2), for its efficient targeting to ER and LD and photosensitization of cancer cells.

RESULTS

Taking clues from the above reports, we rationally designed and synthesized a new class of *bis*-chromophoric fluorescent dyad by fusing naphtholimine-BF_2 at *meso*-linked BODIPY (**N*m*B**) and *β*-linked BODIPY (**N*b*B**) (Figure 1B, C). For synthesis of **N*m*B**, dye **1** was condensed with 2-hydroxy-1-naphthaldehyde to generate Schiff base **2**, which was treated with excess $BF_3{\cdot}OEt_2$ to furnish **3** (**N*m*B**). For **N*b*B**, dye **4** (**BP**) was nitrated to obtain nitro BODIPY (**5**) which on further Zn-mediated reduction afforded 2-amino BODIPY (**6**). Further dye **6** was condensed with 2-hydroxy-1-naphthaldehyde to form corresponding Schiff base, which was treated with excess $BF_3{\cdot}OEt_2$ to furnish **7** (**N*b*B**). The detailed synthesis and data for the characterization of the reaction products are included in Supplementary methods and Figures S1−S6.

UV/vis absorption, fluorescence spectra and photophysical properties of the **N*m*B**, **N*b*B**, and **BP** were evaluated in dicholoromethane (DCM) (Figures 2A and S7, Table S1). All three dyes showed narrow absorption bands with high molar extinction coefficients (ε_{max}). Interestingly, both **N*m*B** and **N*b*B** dyes showed greenish yellow fluorescence but with drastically compromised intensity (Φ_{fl} = 0.04 for **N*m*B** and 0.09 for **N*b*B**, Table S1), as compared to **BP** (Φ_{fl} = 0.99, Table S1). It is important to mention here that the Stokes shift (ν) of the dye **N*b*B** is ∼3 times higher than the **BP** (*vide infra* for explanation). Strikingly, the **N*b*B** shows negative solvatochromism, i.e., hypsochromic shift of the fluorescence absorption maxima in different solvents with increasing dielectric constant.,[30,32] The λ_{em} of **N*b*B** was 514 nm in water, which is red-shifted by 30 nm in cyclohexane (λ_{em} = 544 nm). In contrast, this shift was only 6 nm for **N*m*B** dye (Figures 2B, S8, Table S2, S3), suggesting that linking of naphtholimine-BF_2 derivative at *β*-position of BODIPY may be critical and have profound effect on the self-aggregation-based shift of fluorescence emission of **N*b*B** dye in nonpolar environment. This conclusion was further supported by the observation that yellow fluorescence of **N*b*B** in DCM solution turned to red due to self-aggregation in solid state (Figure 2C, D).

Considering a significant effect of solvent polarity on λ_{em}, it is expected that naphthaolimine moiety in **N*b*B** dye may direct it for (1) ER-specific localization and (2) allow change of intrinsic fluorescence, when it is channelized from ER (polar zone) to LD (nonpolar zone). In order to evaluate such phenomenon, MIA-PaCa-2, pancreatic ductal adenocarcinoma cells were incubated with **BP**, **N*m*B**, and **N*b*B** (30 min) and visualized under confocal laser scanning microscope. The green fluorescence (λ_{ex} = 488 nm) of all three dyes was exclusively localized to the cytoplasm (Figure 3A, B) and the intensity was in the order of **BP** > **N*b*B** > **N*m*B** (Figure 3A−C). Although fluorescence emission of **N*b*B** was lower as compared to **BP**, it was sufficiently high for microscopic studies. In contrast, fluorescence intensity of **N*m*B** was almost 3 folds lesser than **N*b*B** in cells. As shown in Figure 3A−C, **BP**

https://doi.org/10.1021/jacsau.3c00539
JACS Au 2024, 4, 2838−2852

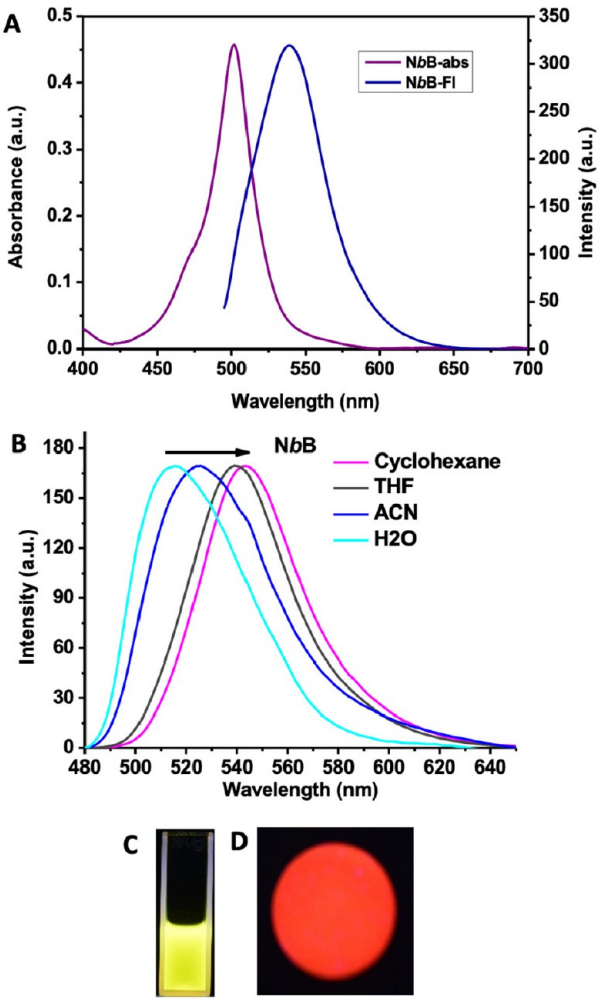

Figure 2. Photophysical properties of **N*b*B**. (A) Absorbance and fluorescence spectra (λ_{ex} = 470 nm) of **N*b*B** in DCM. (B) Fluorescence spectra of **N*b*B** were acquired in different solvents (λ_{ex} = 470 nm, a.u. = arbitrary unit). (C) Fluorescence of **N*b*B** in DCM under UV lamp of higher wavelength (365 nm). (D) Fluorescence of **N*b*B** in solid state (KBr pallet) under UV lamp of higher wavelength (365 nm).

showed single fluorescence (only green) and found to be distributed all over the cytoplasm, including globules, suggesting its nonspecific cellular distribution. Interestingly, both **N*m*B** and **N*b*B** seem to label two separate subcellular structures, including punctae like globules. Of note, **N*m*B** showed single fluorescence (only green) in these two subcellular structures. In contrast, **N*b*B** can simultaneously label two separate subcellular structures with dual colors, as some portion of "green fluorescence" also displayed intense "red fluorescence" in the form of punctae/globule (Figure 3A, B). Further, intracellular localization of **N*b*B** was assessed by analyzing its colocalization with commercially available specific probes for mitochondria (Mito-Tracker Red), lysosomes (Lyso-Tracker Red) and ER (ER-Tracker Red and ER-Tracker Blue). Our analysis on correlation of fluorescence intensities revealed poor colocalization of **N*b*B** with major portions of mitochondria and lysosomes (Figure S9A–D). These results suggested that **N*b*B** may not be primarily localized at mitochondria and lysosomes. Of note, **N*b*B** colocalization was correlated with some portions of mitochondria (*vide infra* Discussion section). Interestingly, cellular green fluorescence of **N*b*B** showed excellent colocalization with commercially available ER-specific probes (ER-Tracker Blue and ER-Tracker Red) at ER and LDs in MIA PaCa-2 cells (Figure S10, S11 A, B, E). Quantitatively, Pearson's coefficient (R= 0.73) for colocalization and correlation of intensity of **N*b*B** with ER-Tracker Red also showed excellent colocalization at different parts of MIA-PaCa-2 (Figure S11 A, B, E). Similar results were also observed in another PDAC cells i.e., PANC-1 (R= 0.70) (Figure S11 C, D, E). Further, localization of **N*b*B** at LDs was analyzed in cells. LDs are globular organelles, which show high refractive index in differential interference contrast image (DIC).[19] In two different cells (MIA-PaCa-2 and PANC-1), **N*b*B** stained red fluorescing punctae almost colocalized precisely with lipid droplets with high refractive index (Figure 3D and S12).[19] Together, these results confirm an efficient localization of **N*b*B** at ER and LDs, when naphtholmine-BF_2 derivative is conjugated at β-position of **BP**. In contrast, **N*m*B** also colocalized substantially with ER Tracker Red (Figure S13), suggesting **N*m*B** may also have some affinity for ER.

We further employed Lambda Scanning Mode (LSM) in confocal microscopy, a powerful tool that employs single λ_{ex} for characterizing fluorescence emission spectrum of the dye in different cellular organelles/locations. LSM acquisition at λ_{ex} (488 nm) revealed that fluorescence emission of **N*b*B** was evident in ER in the range of 505–565 nm (λ_{max} = 531.8 nm; Green region) and significantly drops at >570 nm (Figure 4A–C). Interestingly, fluorescence emission of **N*b*B** was retained significantly in nonpolar LDs in 570–638 nm region. At λ > 585 nm, ER structure specific green fluorescence vanishes drastically while exquisite yellow/red fluorescence of LDs were evident (Figure 4A–C). These fluorescence spectra of **N*b*B** in ER (polar) and LD (nonpolar) region are in excellent agreement with its photophysical properties in solutions (Figure 2B). To further confirm that *in situ* dual florescence properties of **N*b*B** is dependent on the different polar environments in ER and LD, we have performed confocal microscopy based FRAP (fluorescent recovery after photobleaching) assay.[33] In this assay, **N*b*B** fluorescence in the small region of interest (ROI) in ER and LDs were photobleached through microirradiation with high-intensity laser. Subsequently, uptake/diffusion of the **N*b*B** from its surroundings was assessed measuring the kinetics of fluorescence recovery in respective ROIs in live cell imaging. We observed a quick and complete recovery of **N*b*B** fluorescence (green) in ROI in ER (Figure 5A, B). Contrarily and intriguingly, we observed that (1) the fluorescence recovery (yellow fluorescence) was severely affected while (2) green color appeared subsequently in LD (ROI), suggesting the diffusion of aqueous **N*b*B** solution (green), from ER or cytoplasm, into the LD (ROI) without being mixed with nonpolar core of the LD (Figure 5A, C). Together, these results showed a first case of design of a novel synthetic molecule for dual targeting and imaging of cellular ER and LDs.

Further, sensitivity for dual fluorescence and photostability of the **N*b*B** dye for microscope imaging was assessed. Our results revealed that dual fluorescence imaging of ER and LDs was distinctly evident at a concentration as low as 0.5 μM of **N*b*B** (Figure S14A–C). Interestingly, although ER specific green fluorescence was not evident/quantifiable at 0.1 μM of **N*b*B**, LDs specific red fluorescence was still apparent/quantifiable at such low concentration (Figure S14A–C). Moreover, **N*b*B** still retained ~50% of its fluorescence even after acquiring 60 images for 2 h (λ_{ex} = 488 nm) in a laser

https://doi.org/10.1021/jacsau.3c00539
JACS Au 2024, 4, 2838–2852

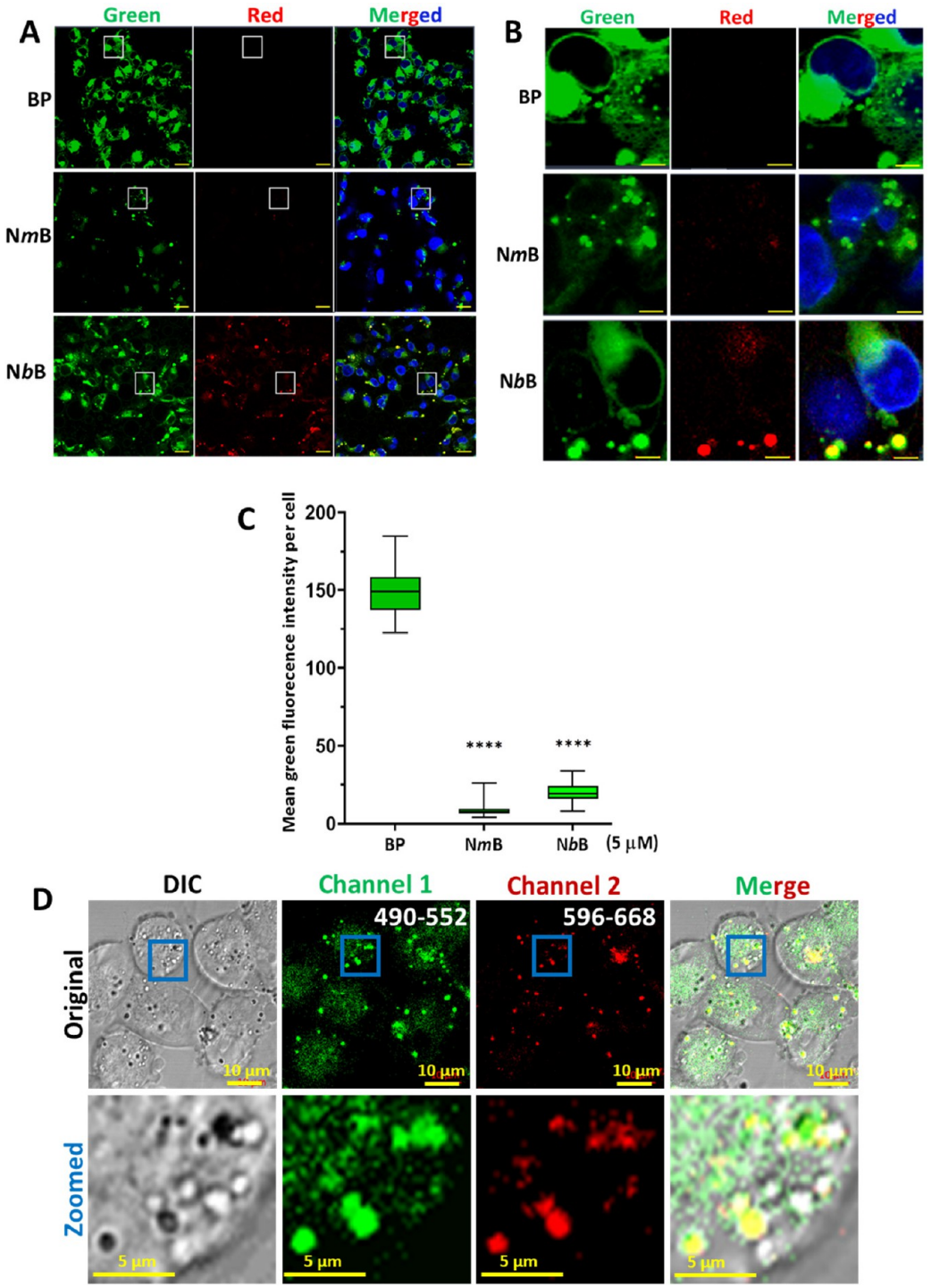

Figure 3. Localization and dual fluorescence properties of **N*b*B** in ER and LD in cancer cells. (A, B) MIA PaCa-2 cells were treated with **BP**, **N*m*B**, and **N*b*B** (5 μM each) for 30 min and fluorescence images were acquired in confocal microscope. Green channel: λ_{ex} = 488 nm, λ_{em} = 490−552 nm; Red channel 2: λ_{ex} = 594 nm, λ_{em} = 596−668 nm), Scale bar = 20 μm in A and 5 μm in B, respectively. (C) Mean green fluorescence intensity of **BP**, **N*m*B**, and **N*b*B** per cell was quantified in channel 1 (green) in the above experiment and plotted. ****$p < 0.0001$ w.r.t **BP** treatment. (D) MIA PaCa-2 cells were treated with **N*b*B** (5 μM) for 30 min and DIC and fluorescence images were acquired in multichannel mode in confocal microscope. The highlighted boxes in the upper panels of images were zoomed to show localization of **N*b*B** in ER (green only) and LDs (yellow color due to colocalization of green in channel 1, red in channel 2 and black in DIC channel for globular lipid droplets). (Channel 1: λ_{ex} = 488 nm; Channel 2: λ_{ex} = 594 nm).

scanning microscope (Figure S15A, B). Moreover, **N*b*B** remained photostable when continuously photoirradiated under tungsten lamp for 2 h (Figure S16A, B). Therefore, **N*b*B** appears to be sensitive dye for simultaneous imaging of ER and LD for sufficiently long time. It tends to lose some of its fluorescence properties after repeated laser irradiations/scanning for longer time, which may be attributable to its PDT effect. In order to understand how **N*b*B** is routed to two different cellular organelles (ER and LD) and their possible interdependence, we followed the kinetics of cellular local-

https://doi.org/10.1021/jacsau.3c00539
JACS Au 2024, 4, 2838−2852

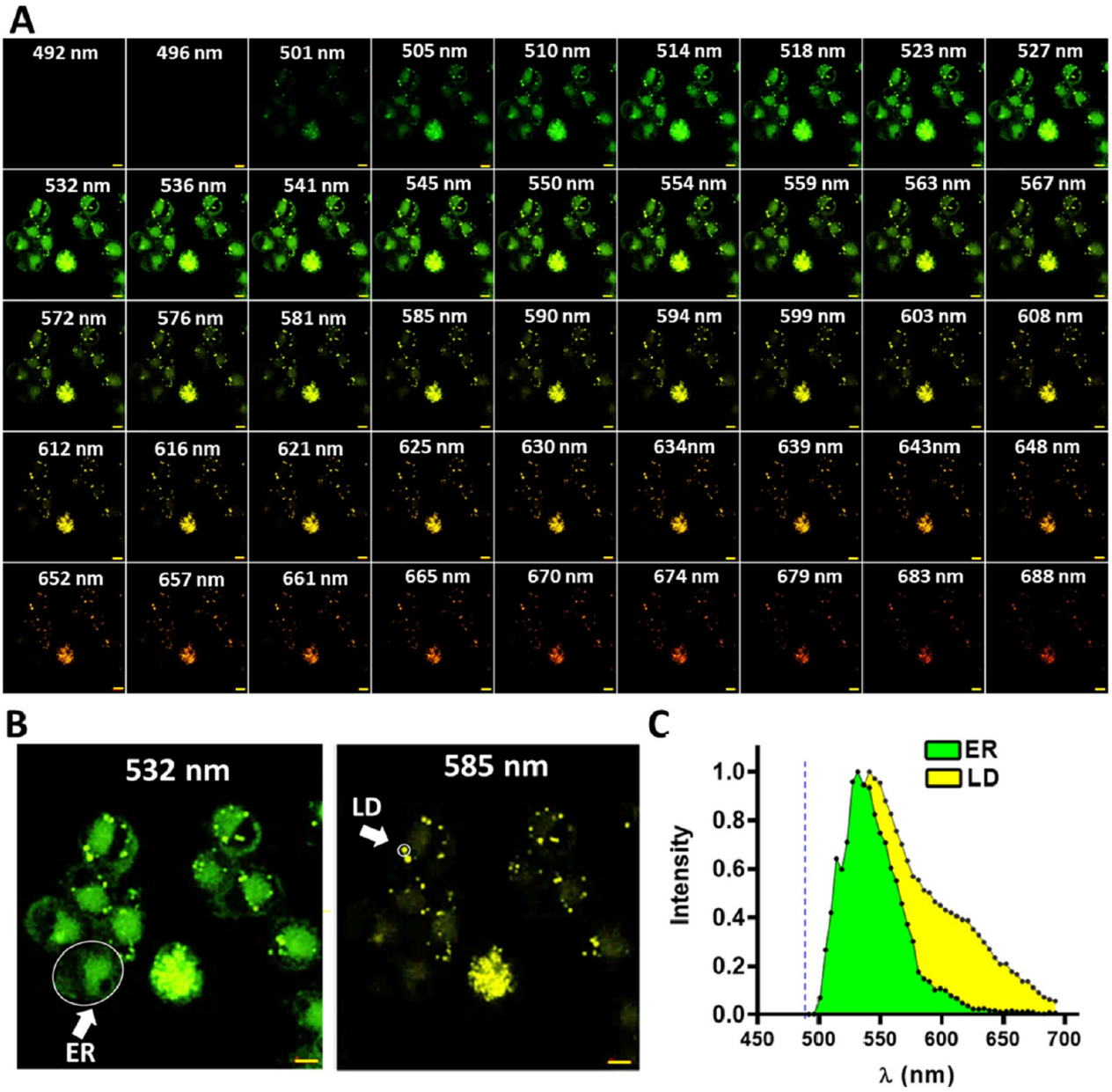

Figure 4. Spectral imaging of **N*b*B** at ER and LD in cells. (A−C) MIA PaCa-2 cells were treated with **N*b*B** (5 μM) for 30 min. *In situ* fluorescence emission of **N*b*B** was acquired in λ-scan mode from 492 to 668 nm at the interval of 4−5 nm (λ_{ex} = 488 nm). Enlarged images showing ER and LD specific dual emissions of **N*b*B** at 532 and 585 nm are shown in "B". Arrows indicate the ROI markings for ER and LD, respectively. Fluorescence emission at the ROI for ER and LD are shown in the form of fluorescence spectra in "C" (Dashed line in the graph = λ_{ex} at 488 nm). Scale bar = 10 μm.

ization of **N*b*B** in MIA-PaCa2 cells, employing live cell confocal imaging. Our data revealed that the fluorescence of **N*b*B** promptly appeared at ER (green) within 4 min of staining and intensified (green) up to 15 min at ER. Subsequently yellow-red colored LDs emerged from the ER (Movie M1, Figure 5D, E). Moreover, formation of yellow-red LD particles was almost confined to ER (green) region, supporting the previous report that biogenesis of LD particles is originated from ER through retrograde ER-LD trafficking process.[19] Of note, the commercial ER-Tracker Red and ER-Tracker Blue also seem to be localized at LD particles (Figure S10, S11), which is difficult to confirm due to its similar fluorescence emission properties at ER and LDs.

After establishing first two properties (localization at ER and LDs and simultaneous dual imaging), we ventured to explore the PDT effects of these novel conjugates. One of the critical requirements of the PDT is efficient T_1 formation and subsequent $^1O_2$ generation for killing cancer cells. The $^1O_2$ generation capacities was determined by monitoring the dye-sensitized photooxidation of 1,3-diphenylisobenzofuran (DPBF) in polar ethanol medium (see supplementary method). Under visible light photoirradiation (>495 nm), **N*b*B** induced $^1O_2$ mediated photooxidation of DPBF, which was assessed by the rapid decay of absorption peak (412 nm) of DPBF (Figure 6A). Imperatively, the order of $^1O_2$ generation/photooxidation capacity was **N*b*B>N*m*B>BP** (Figure S17), suggesting that the triplet conversion of the

https://doi.org/10.1021/jacsau.3c00539
JACS Au 2024, 4, 2838−2852

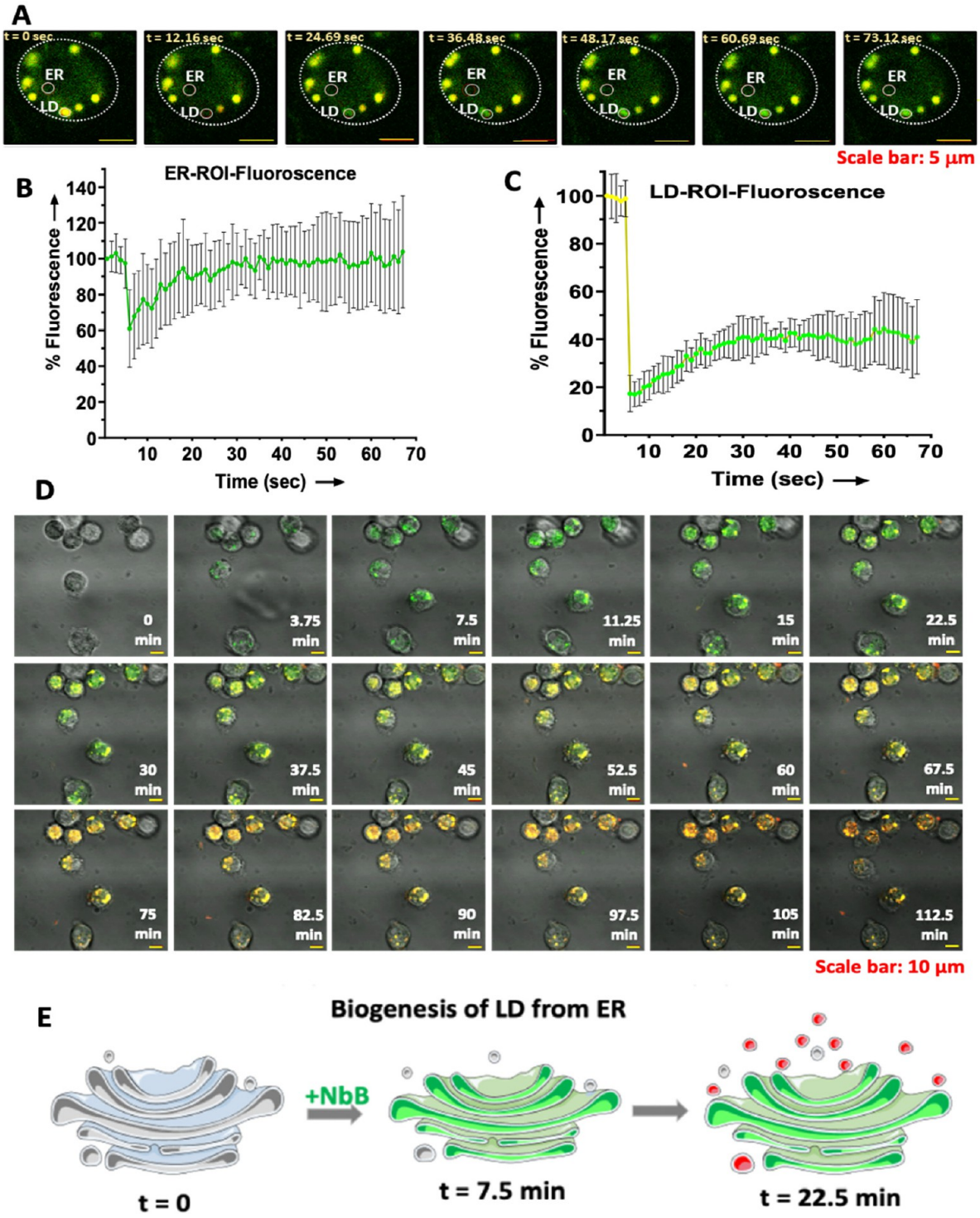

Figure 5. Dual fluorescence properties of **N*b*B** are associated with different polarity in ER and LD. (A-C) Florescence recovery after photobleaching (λ_{ex} = 488 nm) in ROI in ER and LD in MIA PaCa-2 cells were measured, after labeling of cells with **N*b*B** (5 μM, 30 min). (D, E) Scheme and images showing the kinetics of labeling of **N*b*B** (5 μM) in ER and LD organelles in MIA PaCa-2 cells.

N*b*B is very high *vis-à-vis* **N*m*B** and **BP**. Our further analysis showed that $^1O_2$ quantum yield (Φ_Δ)[34,35] of **N*m*B** and **N*b*B** were 0.05 and 0.25, respectively. Φ_Δ of **N*b*B** is comparable with that of previously reported PSs.[36] Although, Φ_Δ of **N*b*B** is relatively lesser than that of Rose Bengal (Φ_Δ = 0.8), a strong PS, precise localization of **N*b*B** at ER and LDs may be helpful in achieving efficient photosensitization of pancreatic cancers. Further, to assess the extent of T_1 formation of all three dyes, nanosecond flash photolysis was used (see methods). As shown in Figure 6B, a strong triplet−triplet absorption signal (425 nm) and very strong bleach at 500 nm was observed for **N*b*B**, while weak/no signal was observed for **N*m*B** and **BP** (7 ns pulse, λ_{ex} = 532 nm). Moreover, this signal of **N*b*B** decays faster in air (lifetime: 0.65 μs) than in nitrogen atmosphere (lifetime: 37 μs) (Figure 6C, D), suggesting efficient transfer of energy from T_1 to generate $^1O_2$. The triplet yield of the **N*b*B**

https://doi.org/10.1021/jacsau.3c00539
JACS Au 2024, 4, 2838−2852

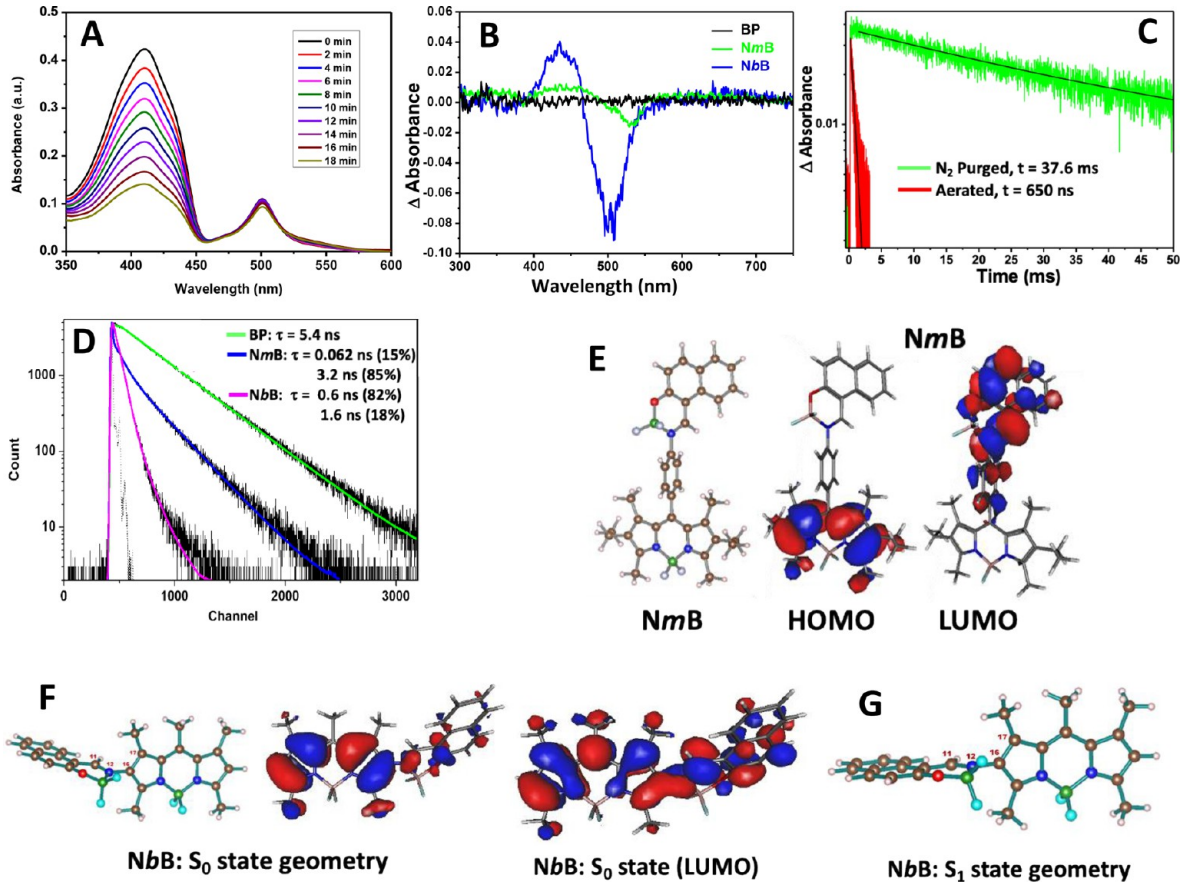

Figure 6. Photophysical and photochemical properties of **N*b*B** as a PDT agent. (A) **N*b*B** (5 μM) mediated photooxidation of DPBF (50 μM), in ethanol, was measured in term of change in absorption spectrum of DPBF during photoirradiation (light source: > 495 nm, a.u.: aribitrary unit). (B) Nanosecond transient absorption spectrum of dyes **BP**, **N*m*B**, and **N*b*B** and (C) triplet decay kinetics of **N*b*B** in dichloromethane (λ_{ex} = 532 nm, λ_{probe} = 425 nm). (D) Emission decay traces (at 550 nm) of the dyes **BP**, **N*m*B**, and **N*b*B** in dichloromethane were measured by TCSPC method. Solid lines are the exponential fit to the experimental data and obtained lifetimes are given in the inset. (E−G) Optimized molecular geometry structures of **N*m*B** and **N*b*B** at the ground and excited states.

was estimated to be ∼60 (±5)% by comparing the bleach signal with platinum octaethylporphyrin, a standard triplet sensitizer, under identical experimental conditions (Figure S18). Despite low fluorescent quantum yield of **N*m*B** and **N*b*B**, only later has the ability to generate high levels of T_1 and $^1O_2$. This anomalous behavior was further explained by theoretical results. Using B3LYP/def-TZVP level of theory, we observed that electron density being completely shifted toward *meso*-naphtholimine-BF_2 moiety in LUMO (lowest occupied molecular orbital) or BODIPY core in HOMO (highest occupied molecular orbital), due to torsion angle in **N*m*B** (Figure 6E). Besides, electron withdrawing nature of *meso*-naphtholimine-BF_2 alters the localization of HOMO and LUMO and hence enhances the nonradiative emission coupled weak fluorescence of **N*m*B**.[36] In contrast, we did not see any charge redistribution as both HOMO and LUMO are located mainly on the BODIPY moiety and slightly spread over the β-naphtholimine-BF_2 moiety in S_0 ground state geometry of **N*b*B** (Figure 6F). Further, its β-naphtholimine-BF_2 and the BODIPY segment are not coplanar and bear a dihedral angle (C11−N12−C16−C17 = 73.6°) between them (Figure 6F). However, the β-naphtholimine-BF_2 moiety in the S_1 excited state was almost orthogonal with the BODIPY core (C11−N12−C16−C17 = 96.7°) (Figure 6G). This geometry relaxation on photoexcitation increases the Stokes shift considerably.[36] This explains and supports the fluorescence quenching of **N*b*B** is due to its efficient conversion to T_1 state. Together, above result confirms the unique ability of **N*b*B** dye for high T_1 and $^1O_2$ yield, which makes **N*b*B** also an excellent PDT candidate.

Considering the above impressive properties of **N*b*B** (ER-LD targeting and high T_1 and $^1O_2$ generation) over **N*m*B** (poor localization in ER-LDs, low $^1O_2$ quantum yield), we sought to know whether **N*b*B** can also able to kill PDAC cells by selectively targeting ER-LD through PDT. As shown in Figure 7A, our results revealed that both **BP** and **N*m*B** were almost completely failed to reduce colonogenic growth of MIA PaCa-2 cells in the absence/presence of light. Interestingly, **N*b*B** could reduce clonogenic growth in a concentration dependent manner (dark toxicity), which was robustly photosensitized in two different PDAC cells (MIA PaCa-2 and PANC-1; Figures 7A−C, S19A−C) in a light dose dependent manner. These results are in agreement with the singlet oxygen generating properties of the **N*m*B**, **N*b*B**, and **BP** (Figure S17). A strong synergistic interaction between **N*b*B** and light was observed for PDT mediated killing of both PDAC cells, as assessed by Combenefit software (Figures 7D, S19C). IC_{50} of **N*b*B** were found to be 1.61 μM and 0.37 μM, at 1 h light dose, for MIA PaCa-2 and PANC-1 cells, respectively. Phototoxic index (PI), i.e., IC_{50} in dark/IC_{50} in light, of **N*b*B** (60 min photoirradiation) were found to be 2.91 and 14.16 for

https://doi.org/10.1021/jacsau.3c00539
JACS Au 2024, 4, 2838−2852

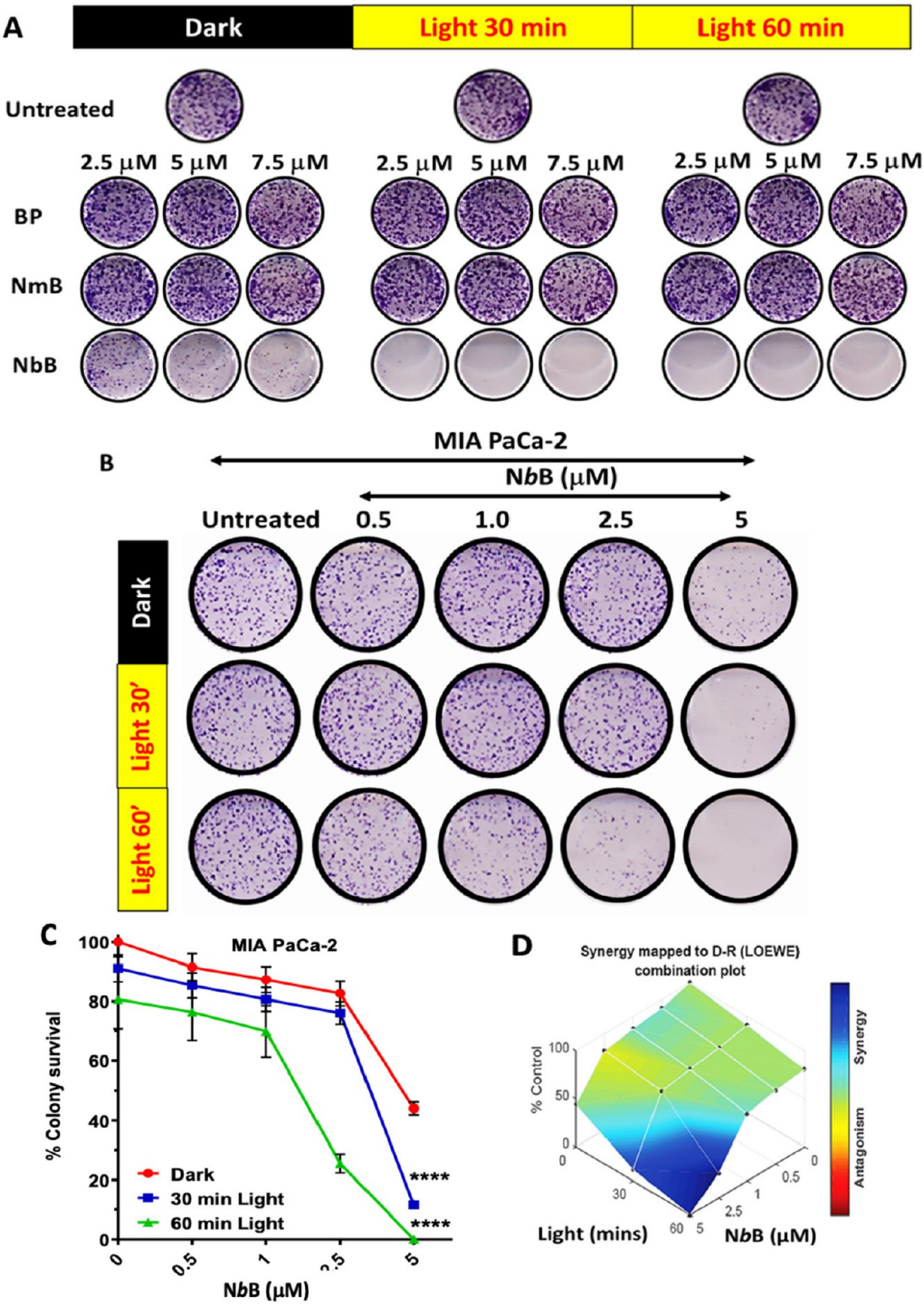

Figure 7. N*b*B efficiently photosensitizes pancreatic cancer in a concentration dependent manner. (A) MIA PaCa-2 cells were treated with different concentration of **BP**, **N*m*B**, and **N*b*B** for 30 min and exposed to visible light. Clonogenic survival was assessed after 9−10 days of treatments. (B−D) MIA PaCa-2 cells were treated with **N*b*B**, as mentioned above, at lower concentrations and clonogenic survival was assessed. Representative images of clonogenic assay are shown in "B". Quantification for the colony growth and Comebenfit based synergism (**N*b*B** and light) are shown in "C" and "D", respectively. ****$p < 0.0001$ w.r.t, respective, **N*b*B** concentration under dark.

MIA PaCa-2 and PANC-1 cells, respectively. Similar ranges of PIs are also reported for recently developed PSs.[37,38] In order to assess PDT effects of **N*b*B** on nonpancreatic cancer and normal cells, photosensitization effects of **N*b*B**, on CAL-33 (squamous cell carcinoma), HeLa (cervical carcinoma), DLD-1 (colorectal adenocarcinoma), and MCF-10A (normal mammary epithelial) cells was also assessed. Interestingly, our results showed the PDT effects of **N*b*B** was less pronounced in nonpancreatic cells (Figure S20, Table S4) *vis-à-vis* pancreatic cancer cells (*vide infra* Discussion section). For PDAC cells, similar photosensitization effects were also observed for short-term MTT assay (Figure S21A, B). In contrast to long-term clonogenic assay, the loss of cell viability was higher for Mia PaCa-2 than PANC-1 cells in short-term

https://doi.org/10.1021/jacsau.3c00539
JACS Au 2024, 4, 2838−2852

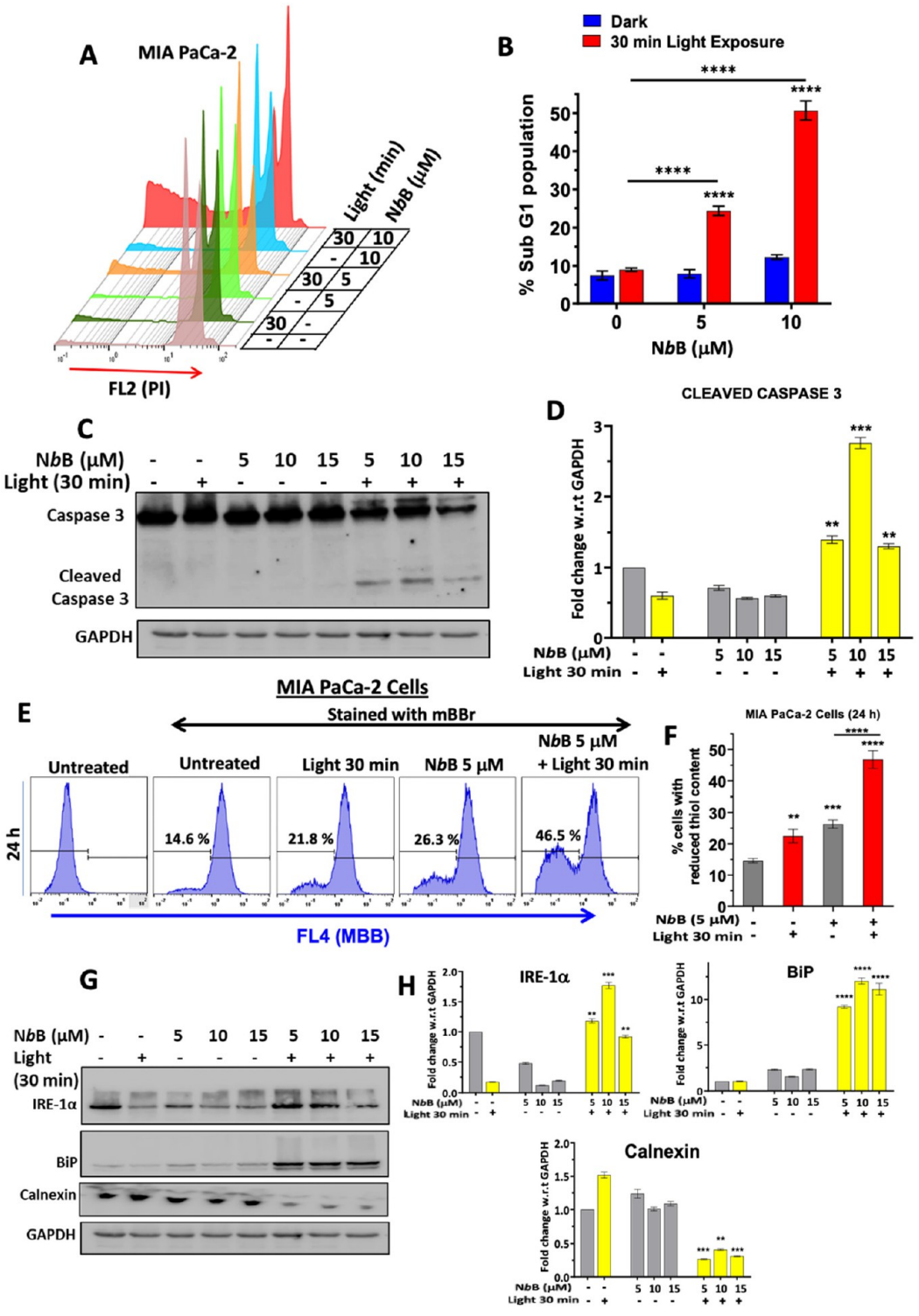

Figure 8. N*b*B induces ER stress and apoptosis in pancreatic cancers. (A, B) MIA PaCa-2 cells were treated with different concentration of **N*b*B** for 30 min and exposed to visible light. Apoptosis was assessed by sub-G1 assay after 24 h of treatments. Quantifications for% sub-G1 in different treatments are shown in "B", ****$p < 0.0001$. (C, D) MIA PaCa-2 cell were treated with **N*b*B** as above and activation of caspase-3 was assessed by Western blotting and quantified. **$p < 0.01$ and ***$p < 0.001$ w.r.t respective **N*b*B** concentration under dark. (E, F) MIA PaCa-2 cell were treated with **N*b*B** and light as above and cellular thiol level was assessed by MBB based flow cytometry assay. **$p < 0.01$, ***$p < 0.001$, ****$p < 0.0001$ w.r.t untreated cells. (G, H) MIA PaCa-2 cell was treated with **N*b*B** and light as above and ER stress markers are assessed by Western blotting and quantified. **$p < 0.01$ and ***$p < 0.001$ w.r.t respective **N*b*B** concentration under dark.

MTT assay (48 h) in response to the photosensitizing effects of **N*b*B**. The variation of the results between clonogenic and MTT assay may be attributable to the fact that MTT assay shows loss of cell viability due to reduced metabolism and does not accounts growth arrest and different types of cell death. In contrast, clonogenic assay is considered as the "gold standard", because this assay accounts the final outcomes of all types of cell death, including delayed growth arrest.[39] Hence, the higher

https://doi.org/10.1021/jacsau.3c00539
JACS Au 2024, 4, 2838−2852

N*b*B induced photosensitivity in PANC-1 cells, in clonogenic assay, may be attributable to some of the delayed cellular effects.

Since **N*b*B** showed much superior PDT effects than **N*m*B**, further studies were carried out with **N*b*B** to unravel its molecular mechanism behind photosensitization of cancer. Mechanistically, The PDT effect of **N*b*B** is mediated through induction of sub-G1 and cleavage of caspase-3, the markers of apoptosis, in PDAC cells (Figures 8A−D, S22). Since **N*b*B** targets ER and LDs and has the ability to generate copious amount of $^1O_2$ in the presence of light, PDT effects of **N*b*B** might be attributable to induced ER stress and LD damage. Recent reports show that ER stress culminates to ROS (reactive oxygen species) generation and glutathione (GSH) depletion, leading to cell death.[40,41] We could not able to assess the generation of cellular ROS in **N*b*B** mediated PDT process, as fluorescence spectrum of the **N*b*B** interferes with commercially available ROS analyzing dyes (DCFDA, DHE, etc.). Alternatively, we have analyzed GSH level by monobromobimane (MBB), which emits blue florescence after reacting with cellular GSH. In this regard, treatment of MIA PaCa-2 and PANC-1 cells with **N*b*B** led to significant reduction of cellular GSH in a time dependent manner (Figure 8E, F, S23A−C, S24A−C). In contrast, **N*b*B** or light alone treatment failed to induce such significant changes in PDAC cells. Imperatively, PDT treatment with **N*b*B** significantly affected the expression of ER-stress markers e.g., IRE-α and BiP levels were increased while Calnexin level was reduced (Figure 8G, H). Since our results also showed that **N*b*B** can be localized to LDs (Figure 5, S10, S11, Movie M1), further we sought to know whether **N*b*B** may have the propensity to photodamage LDs through the generation of $^1O_2$ in nonpolar lipid medium of LDs. In this regard, the $^1O_2$ generation capacities of **N*b*B** in cyclohexane (nonpolar) and ethanol (polar) medium was assessed in DPBF assay (see method section). It was observed that the photooxidative degradation of DPBF in the presence of **N*b*B** was higher in cyclohexane as compared to that in ethanol (Figure S25A, B). Hence the $^1O_2$ generation effect of **N*b*B** is more in nonpolar medium as compared to that in polar medium (*vide infra* discussion section). At cellular level, **N*b*B** mediated photodamage and lipid peroxidation level were assessed by measuring lipid peroxide using Liperfluo dye in flow cytometry assay.[42] As shown in Figure S25C, D, **N*b*B** significantly enhanced lipid peroxidation in MIA PaCa-2 cells, immediately after light exposure, suggesting that localization of **N*b*B** at LDs may cause photodamage to LDs and contribute to its PDT mediated killing of PDAC cells.

DISCUSSION

Recently, several reports emphasized on the importance of PDT agents for targeting ER in cancer. For example, Hypercin is reported to accumulate and generate ROS in ER, and photosensitize cancer cells.[43] Redaporfin targets the endoplasmic reticulum and Golgi apparatus and shows its PDT effects though its direct antineoplastic action and indirect immune-dependent destruction of malignant lesions.[44] Another important cellular component, lipid droplets (LDs) are closely associated with ER. LDs are cytosolic lipid storing organelle, which also contribute to the maintenance of ER membrane and homeostasis.[45] It is challenging to develop a photosensitizer, which can precisely target ER and LDs and also show dual fluorescence for imaging ER and LD simultaneously.

In the current investigation, we describe a design and synthesis of a novel photosensitizer, where naphtholimine-BF_2 was conjugated at *meso*-linked BODIPY (**N*m*B**) or β-linked BODIPY (**N*b*B**). Although few reports showed naphthalene derivatives have the ability to elicit ER stress and localize to stain the membranous structures, including ER,[23−25,46] its role as a specific targeting agent to global pool of cellular ER and LDs is largely unknown. Our extensive microscopic characterization of **N*b*B** along with different organelle specific commercial dyes revealed that, napathalene derivative, i.e., naphtholimine-BF_2 conjugation at β-linked BODIPY (**N*b*B**) can precisely target it to global pool of cellular ER. **N*b*B** poorly localized to lysosomes while its colocalization with a small pool of mitochondria was also observed (Figures S9−11), which may be attributable to close association of ER with mitochondria at different cellular sites.[47] Of note, **N*m*B** molecule, where naphtholimine-BF_2 was conjugated at *meso*-linked BODIPY, also showed some affinity for ER (Figure S13), suggesting naphthalene moiety has the potential to be localized to ER. During LD biogenesis, natural lipids accumulate in the ER membrane and coalesce into lenses/blisters, which eventually grows into nascent LDs at the interface of ER membrane and cytoplasm.[48] Commercially available ER Tracker Green/Red stains both ER and LDs with single fluorescence color (Figure S11).[49] ER Tracker Green/Red have hydrophobic glibenclamide moiety, which binds to ER membrane protein (sulfonylurea receptors of ATP-sensitive K+ channels). During LD biogenesis from ER membrane, these ER membranes bound dyes may be sequestered to nonpolar zone in LDs. In the current investigation, **N*b*B** strikingly showed simultaneous dual fluorescence in ER (green) and LDs (green and red) at single excitation wavelength (Figure 4). Furthermore, excitation at 488 nm showed **N*b*B** stained ER (green) and LDs (green and red), while excitation at 594 nm exclusively revealed **N*b*B** staining in lipid droplets (LDs) (red), thereby providing a discrete differentiation between **N*b*B**-stained ER and LDs (Figure 3, S12). Owing to the hydrophobic napatholamine core, **N*b*B** may possibly binds with some of the ER membrane proteins and may exists in relatively more hydrated liquid disordered phase in ER membrane. Over a period, **N*b*B** sequesters to LDs during LD biogenesis. Indeed, our live imaging studies revealed that **N*b*B** is rapidly cell permeabilized and appeared on ER (green) within 5 min, subsequently **N*b*B** stained yellow-red colored LDs were appeared from ER (∼22 min) (Movie M1, Figure 5D, E). These data support the notion that **N*b*B** is primarily localized to ER membrane initially and subsequently channelized to LDs during LD biogenesis process. Dual fluorescence of **N*b*B** in ER and LD is attributable to its change in its photophysical properties in polar and nonpolar medium. Kanvah et al. observed conjugation of pentafluorophenyl group to naphthalene enhances its aggregation induced enhancement (AIE) of intensity and bathochromic shift of fluorescence maxima in polar medium.[50] Bhosale et al. reported synthesis of amide group conjugated naphthalene diimide, which shows aggregation-induced emission enhancement (AIEE) in the presence of nonpolar medium.[51] Hence, aggregation property of naphthalene is differentially affected by the appended moiety, leading to notable solvatochromic shift. In our case, **N*b*B** but not **N*m*B** showed profound effect on the self-aggregation-based shift of fluorescence emission in nonpolar environment (Figure 2B, S8, Table S2, S3) or solid state (Figure 2C, D). Together, our findings suggested that

https://doi.org/10.1021/jacsau.3c00539
JACS Au 2024, 4, 2838−2852

napathalene derivative, i.e., napthaolmine-BF_2 at β-position of BODIPY is imperative to (1) target **NbB** to the ER and LDs and (2) show the aggregation induced dual fluorescence of **NbB** in ER (green) and LDs (red), owing to solvatochromic shift in these two subcellular organelles. Above properties along with minimal dark cytotoxicity (Figures 7, S19) and photostability (Figure S15) positions **NbB** as an excellent imaging tool for assessing dynamics of subcellular ER and LDs.

Emerging evidence suggested that subtle redox imbalance in ER and/or LD damage elicit ER-stress mediated death process in cancer cells. In view of this, recently several studies were focused on developing ER organelle specific PDT agents.[52−54] Moreover, considering the importance of LDs in ER homeostasis and cell survival, Chen et al. developed first photosensitizer (MNBS), which selectively localized to LD and induces cellular lipid peroxidation mediated cell death upon irradiation.[55] However, these organelle specific PDT agents normally target either ER or LDs to induce cell death. Here in, we report **NbB** as a first photosensitizer, which can precisely localize and photodamage both ER and LDs to induce ER stress and cellular lipid peroxidation. Since pancreatic ductal carcinoma cells (PDAC) are heavily dependent on ER and LDs, we have used two different PDAC cells (MIA PaCa-2 and PANC-1) as a model system in the current investigation to assess PDT effects of **NbB**. Our results showed that **NbB** induces efficient photokilling and reduces colony formation in PDAC cells (Figures 7, 8, S19, S21, S22). **NbB** mediated PDT effect is less pronounced in nonpancreatic cancers and normal cells at 30 min photoirradiation (Figure S20, Table S4). Of note, these nonpancreatic cells were also sensitive to PDT effects of **NbB**, at higher dose of photoirradiation (60 min, data not shown). These results suggested that PDAC cells were hypersensitive, due to their over reliance on ER-LD, while other cancers may require higher dose of **NbB** and/or photoirradiation for efficient photosensitization. Mechanistically, **NbB** reduces cellular antioxidant (GSH) and induces robust ER stress and lipid peroxidation, supporting its role in organelles specific photodamage of ER and LDs in PDAC cells (Figures 8, S23−25). **NbB** generates $^1O_2$ efficiently in polar and nonpolar medium with higher efficiency in later (Figures 6, S25A, B). **NbB** mediated production of $^1O_2$ is attributable to its ability to generate high levels of T_1 state (Figure 6). Further, our theoretical calculation revealed that orthogonal positioning of β-naphtholimine-BF_2 moiety with BODIPY core enable relaxation of photoexcited **NbB**, leading to increase in Stokes shift and conversion to T_1 state for efficient generation of $^1O_2$ (Figure 6). Higher **NbB** mediated $^1O_2$ generation in nonpolar solvent may be attributable to longer lifetime of $^1O_2$ in nonpolar medium than polar solvent. Moreover, localization of **NbB** in LD structure at high density within the hydrophobic core, which generally overcomes photoquenching of the dye by water.[56] Considering these aspects, **NbB** may likely generates $^1O_2$ efficiently in lipid core of LDs. This is evident from the results showing rapid **NbB** mediated increase in cellular lipid peroxidation upon photoirradiation (Figure S25C, D). Together, **NbB** mediated photosensitization of both ER and LD organelles may offer a new strategy of precision photodynamic therapy for pancreatic cancer.

CONCLUSIONS

In conclusion, this work illustrates for the first time a novel BODIPY based dyad (**NbB**) with three biological functions: (1) precise targeting to ER and LDs, (2) simultaneous dual fluorescence imaging of ER and LD at single excitation wavelength and (3) potent PDT effects on both ER and LDs for sensitization of pancreatic cancer. Interestingly, Rizvi et al. have used two liposomal formulations, encapsulating Visudyne (clinically approved) and lipid derivative of benzoporphyrin for simultaneous photodamage to mitochondria, ER and lysosomes at single wavelength excitation.[57] This formulation of two different PS enhanced PDT effects in ovarian cancer. To date an efficient photosensitization of PDAC through precise and simultaneous targeting of both ER and LD with single agent is not known. Based on several reports, PDT is emerging as a viable approach for treatment of pancreatic tumors.[58] Moreover, advanced fiber optic based light delivery has facilitated the PDT treatment at pancreatic sites.[58] Since, PDAC cells are over-reliant on ER network for hormonal secretion, understanding of comprehensive targeted PDT effect on ER and LDs may help in developing efficient therapy against pancreatic tumors.

MATERIALS AND METHODS

Materials

For organic synthesis, all the chemical reagents and solvents were purchased from a local supplier and were used without any further purification. Fetal bovine serum (FBS), Antibiotic-Antimycotic solution (#15240096), Dulbecco's Modified and Eagle Medium (DMEM) were procured from Gibco, 3-(4,5-dimethylthiazol-2-yl)-2,5-diphenyltetrazolium bromide (MTT, #M5655), propidium iodide (PI), crystal violet, RNase, Hoechst 33342, monobromobimane (MBB), and anti-GAPDH (#G8795) were from Sigma-Aldrich Chemicals. MitoTracker Red, ER-Tracker Red, ER-Tracker Blue, and Lyso-Tracker Red are from Invitrogen. Anticaspase-3 (#CST-9662), anti-IRE-1α (#CST-3294), anti-BiP (#CST-3177), and Calnexin-C5C9 (#2679) were purchased from Cell Signaling Technology. Lumi-Light ECL-plus Western blotting kit was from Roche Applied Science.

Synthesis and Characterization

A detail protocol for the synthesis of the studied molecules is mentioned on the Supporting Information.

Photophysical Properties

Measurement of fluorescence lifetime of the samples dissolved in desired solvents were carried out by time correlated single photon counting (TCSPC) technique using IBH-UK (Horiba-Jobin Yvon) system. 511 nm laser light with a fwhm of about 100 ps was used for excitation of samples and the emission kinetic traces were collected at emission peak. The kinetic traces were fitted exponentially using the IBH DAS 6.2 software module. Triplet spectra and kinetics of the samples were measured by laser flash photolysis technique using a laser kinetic spectrometer (Edinburgh Instruments, U.K.; model LP920). Samples were excited by a 7 ns Nd:YAG laser at 532 nm (second harmonic of 1064 fundamental laser) and probed with a 450 W pulsed xenon lamp. All spectroscopic measurements were carried out at room temperature.

Cell Culture

Pancreatic Ductal Adenocarcinoma (PDAC) cell lines MIA PaCa-2, PANC-1, and other cell lines (HeLa, DLD-1, CAL-33, and MCF10A) purchased from the European Collection of Authenticated Cell Cultures (ECACC), were maintained as per the instruction provided by ECACC. The cell lines were cultured in DMEM having 2 mM glutamine, supplemented with 10% Fetal bovine serum (FBS) and 1% Antibiotic-Antimycotic solution. Cells were grown in a 5% CO_2 and 95% humidity environment at 37 °C temperature. All the experiments were performed within 6−8 passages from the thawing of a cell line from liquid nitrogen.

https://doi.org/10.1021/jacsau.3c00539
JACS Au 2024, 4, 2838−2852

Photoexposure Protocol

The cells were irradiated with white light from a Tungsten filament bulb (400−800 nm, Philips make). Photoirradiation was done for two different time points (30 and/or 60 min). The distance between the surface of irradiated cells and the bulb was 25 cm. The fluence rate was 9.34 mW/cm^2, and radiant exposures were 16.81 J/cm^2 and 33.62 J/cm^2 for 30 and 60 min, respectively.

Clonogenic Assay

Clonogenic assay was performed for the evaluation of the cytotoxic effect of the compound, following report[59] with minor modifications. Briefly, cells (MIA PaCa-2, PANC-1, HeLa, DLD-1, CAL-33, and MCF10A) were seeded (0.8×10^3/well) in 6 well plates in a complete medium for overnight. Cells were treated with **N*b*B** and light as mentioned above and incubated for 8−10 days. Post incubation, cells were washed with PBS, colonies were fixed with chilled methanol for 10 min, and colonies were stained with a 0.5% (w/v) crystal violet solution (30 min). Staining solutions were discarded and washed 3−4 times with water. Stained colonies containing more than 30 cells each were counted under an inverted light microscope. The phototoxic index (PI) values of **N*b*B** were calculated as the ratio of the IC_{50} in the dark to the IC_{50} in the light

Confocal Microscopy

Cells were seeded on a glass coverslip (1×10^5 cells/coverslip) for overnight. Cells were incubated with different concentrations of florescent dyes (**N*m*B**, **N*b*B**, and **BP**) for the indicated time periods. Postincubation cells were washed twice with PBS and then mounted with 80% glycerol before imaging through the confocal microscope (LSM780, Carl Zeiss). For **N*m*B**, **N*b*B**, and **BP**, images were acquired by laser excitation at 488/543/594 nm while Hoechst 33342 was excited with 355 nm laser. For colocalization studies, cells were incubated with **N*b*B** (5 μM) and LysoTracker Red (100 nM) or MitoTracker Red (200 nM) or ER-Tracker Red (500 nM) or ER-Tracker Blue (300 nM) for 20 min. Postincubation, cells were washed twice with PBS and then mounted with 80% glycerol before imaging through the confocal microscope (Zeiss, LSM780). ER-Tracker Red, MitoTracker Red, LysoTracker Red, or ER-Tracker Blue was excited using 594/355 nm laser. Fluorescence intensity and colocalization parameters were assessed using Zen software (Carl Zeiss).

Live Cell Imaging, N*b*B Photostability, and In Situ Lambda Scan Imaging

Live cell imaging and lambda mode scanning of the stained cells were carried out with the confocal microscope (LSM 780, Carl Zeiss), which has an in-built cell incubation chamber (5% CO_2 and 95% humidity) for carrying out live cell imaging experiments for long hours. Cells were seeded on to the thin glass bottom (35 mm) of confocal dishes (SPL Life Sciences #100350) for overnight. Cells were treated with **N*b*B** (5 μM) and kinetics of appearance of fluorescence of **N*b*B**, from 0 to 115 min at the interval of 3.75 min, in cells were acquired in channel 1 (λ_{ex} = 488 nm; λ_{em} = 490−552 nm) and channel 2 (λ_{ex} = 594 nm; λ_{em} = 596−668 nm). For assessing photostability of **N*b*B**, cells were treated as mentioned above and images were acquired continuously in channel 1 (green) for 2 h, at the interval of 2 min (Channel 1: λ_{ex} = 488 nm; λ_{em} = 490 to 588 nm). For in situ lambda scan imaging, cells were treated as above in confocal dishes and spectral imaging in lambda scan mode was carried out in LSM 780 microscope. The **N*b*B** dye was excited at 488 nm and spectral imaging (fluorescence emission) was acquired at every 4−5 nm from 492 to 688 nm.

Fluorescence Recovery After Photobleaching (FRAP) Assay

This assay was carried out as per our previous report for FRAP experiments,[33] with minor modifications. Briefly, Cells were seeded on to the thin glass bottom of confocal dishes for overnight. Cells were treated with **N*b*B** (5 μM, 30 min) and FRAP assay was carried out in LSM 780 confocal microscope. Images were captured using a 6× digital zoom and a 40× magnification to make sure a 1 ms pixel dwell time. The region of interest (bleach ROI in ER and LD) was bleached using 100% power of 488 nm laser line for 40 repetitions after five prebleach photos (488 nm laser line, 1% power) were taken. In addition, photobleaching was taken into consideration during image capture by using a reference region of interest. A total of 100 pictures were taken after bleaching at intervals of one millisecond. Utilizing Zen Blue 3.4 software, the % recovery of **N*b*B** fluorescence was measured after picture acquisition. The formula shown below was employed to determine the percentage of fluorescence recovery:

$$\%\text{recovery at time } t = \left[\frac{\left\{ \frac{\text{MFI of bleach ROI}}{\text{MFI of reference ROI}} \right\}\text{at time } t}{\left\{ \frac{\text{MFI of bleach ROI}}{\text{MFI of reference ROI}} \right\}\text{at time } 0} \right] \times 100$$

MFI stands for mean fluorescence intensity in this context. Data on percentage recovery was used to generate recovery graphs.

Dye sensitized photo-oxidation study,[60] synergistic interaction study (comebenefit),[61] MTT,[62] sub-G1,[63] cellular protein thiol estimation,[64] lipid peroxidation experiment,[42] Western blotting,[64] and computational methodologies[65−68] are performed as per the previous reports. Detailed protocols with minor modifications are included in the Supporting Information.

Statistical Analysis

At least three independent experiments were carried out, and each individual experiment was done in triplicate. GraphPad Prism 8 was used to create all the generated graphs and conduct the statistical analysis. The statistical significance of the data was examined using the unpaired *t* test and analysis of variance (ANOVA). Significant was defined as a probability value of $p < 0.05$. Cells that had been exposed to the vehicle were regarded as untreated controls.

■ ASSOCIATED CONTENT

Supporting Information

The Supporting Information is available free of charge at https://pubs.acs.org/doi/10.1021/jacsau.3c00539.

Detailed experimental procedures and characterization: ^{1}H NMR, ^{13}C NMR, HRMS; additional figures (PDF)

Live cell BODIPY (AVI)

■ AUTHOR INFORMATION

Corresponding Authors

Birija Sankar Patro − *bel>aBio-Organic Division, Bhabha Atomic Research Centre, Trombay, Mumbai 400085, India; Homi Bhabha National Institute, Anushaktinagar, Mumbai 400094, India;* orcid.org/0000-0001-9161-5913; Email: bisank@barc.gov.in

Soumyaditya Mula − *bel>aBio-Organic Division, Bhabha Atomic Research Centre, Trombay, Mumbai 400085, India; Homi Bhabha National Institute, Anushaktinagar, Mumbai 400094, India;* orcid.org/0000-0001-5970-1184; Email: smula@barc.gov.in

Authors

Nitish Chauhan − *bel>aBio-Organic Division, Bhabha Atomic Research Centre, Trombay, Mumbai 400085, India; Homi Bhabha National Institute, Anushaktinagar, Mumbai 400094, India*

Mrunesh Koli − *bel>aBio-Organic Division, Bhabha Atomic Research Centre, Trombay, Mumbai 400085, India; Homi Bhabha National Institute, Anushaktinagar, Mumbai 400094, India*

Rajib Ghosh − *Homi Bhabha National Institute, Anushaktinagar, Mumbai 400094, India; Radiation and Photochemistry Division, Bhabha Atomic Research Centre, Trombay, Mumbai 400085, India*

https://doi.org/10.1021/jacsau.3c00539
JACS Au 2024, 4, 2838−2852

Ananda Guha Majumdar − *bel>aBio-Organic Division, Bhabha Atomic Research Centre, Trombay, Mumbai 400085, India; Homi Bhabha National Institute, Anushaktinagar, Mumbai 400094, India*
Ayan Ghosh − *Laser and Plasma Technology Division, Bhabha Atomic Research Centre, Trombay, Mumbai 400085, India;* orcid.org/0000-0002-1088-1409
Tapan K. Ghanty − *Homi Bhabha National Institute, Anushaktinagar, Mumbai 400094, India; l>eBio-Science Group, Bhabha Atomic Research Centre, Trombay, Mumbai 400085, India;* orcid.org/0000-0001-7434-3389

Complete contact information is available at: https://pubs.acs.org/10.1021/jacsau.3c00539

Author Contributions

‡N.C. and M.K. contributed equally. N.C., M.K., S.M., and B.S.P. conceptualized and designed experiments. M.K. and S.M. synthesized the molecules and performed photophysical studies. R.G. performed nanosecond transient studies. A.G. and T.K.G. performed the theoretical studies. N.C., A.G.M., and B.S.P. executed the biological experiments. B.S.P. prepared the initial draft of the manuscript after taking inputs from all the authors. S.M. and B.S.P. finalized the manuscript. CRediT: **Nitish Chauhan** data curation, formal analysis, investigation, methodology, software, validation, visualization, writing-review & editing; **Mrunesh Koli** data curation, formal analysis, investigation, methodology, software; **Rajib Ghosh** data curation, formal analysis, investigation, methodology; **Ananda Guha Majumdar** investigation, methodology, validation; **Ayan Ghosh** investigation, methodology, software, writing-review & editing; **Tapan K. Ghanty** investigation, methodology, validation; **Soumyaditya Mula** conceptualization, data curation, formal analysis, investigation, methodology, validation, writing-review & editing; **Birija Sankar Patro** conceptualization, data curation, formal analysis, funding acquisition, investigation, methodology, project administration, resources, supervision, validation, visualization, writing-original draft, writing-review & editing.

Funding

This work is funded by intramural funding of Department of Atomic Energy, India.

Notes

The authors declare no competing financial interest.

■ ACKNOWLEDGMENTS

This work is supported financially by Department of Atomic Energy, India. The authors wish to express their gratitude to Ms. Archita Rai for generously providing the Liperfluo dye, necessary for the lipid peroxidation experiment.

■ REFERENCES

(1) McGuigan, A.; Kelly, P.; Turkington, R. C.; Jones, C.; Coleman, H. G.; McCain, R. S. Pancreatic Cancer: A Review of Clinical Diagnosis, Epidemiology, Treatment and Outcomes. *World J. Gastroenterol* **2018**, *24* (43), 4846−4861.
(2) Hilmi, M.; Delaye, M.; Muzzolini, M.; Nicolle, R.; Cros, J.; Hammel, P.; Cardot-Ruffino, V.; Neuzillet, C. The immunological landscape in pancreatic ductal adenocarcinoma and overcoming resistance to immunotherapy. *Lancet Gastroenterol Hepatol.* **2023**, *8* (12), 1129−1142.
(3) Oyadomari, S.; Araki, E.; Mori, M. Endoplasmic Reticulum Stress-Mediated Apoptosis in Pancreatic Beta-Cells. *Apoptosis* **2002**, *7* (4), 335−345.
(4) Jackson, C. L. Lipid Droplet Biogenesis. *Curr. Opin Cell Biol.* **2019**, *59*, 88−96.
(5) Li, J.; Gu, D.; Lee, S. S.-Y.; Song, B.; Bandyopadhyay, S.; Chen, S.; Konieczny, S. F.; Ratliff, T. L.; Liu, X.; Xie, J.; Cheng, J.-X. Abrogating Cholesterol Esterification Suppresses Growth and Metastasis of Pancreatic Cancer. *Oncogene* **2016**, *35* (50), 6378−6388.
(6) Sunami, Y.; Rebelo, A.; Kleeff, J. Lipid Metabolism and Lipid Droplets in Pancreatic Cancer and Stellate Cells. *Cancers (Basel)* **2018**, *10* (1), 3.
(7) Bown, S. G.; Rogowska, A. Z.; Whitelaw, D. E.; Lees, W. R.; Lovat, L. B.; Ripley, P.; Jones, L.; Wyld, P.; Gillams, A.; Hatfield, A. W. R. Photodynamic Therapy for Cancer of the Pancreas. *Gut* **2002**, *50* (4), 549−557.
(8) Huggett, M. T.; Jermyn, M.; Gillams, A.; Illing, R.; Mosse, S.; Novelli, M.; Kent, E.; Bown, S. G.; Hasan, T.; Pogue, B. W.; Pereira, S. P. Phase I/II Study of Verteporfin Photodynamic Therapy in Locally Advanced Pancreatic Cancer. *Br. J. Cancer* **2014**, *110* (7), 1698−1704.
(9) Zhang, C.-J.; Cai, X.; Xu, S.; Zhan, R.; Jien, W.; Liu, B. A Light-up Endoplasmic Reticulum Probe Based on a Rational Design of Red-Emissive Fluorogens with Aggregation-Induced Emission. *Chem. Commun.* **2017**, *53* (78), 10792−10795.
(10) Huang, C.; Li, T.; Liang, J.; Huang, H.; Zhang, P.; Banerjee, S. Recent Advances in Endoplasmic Reticulum Targeting Metal Complexes. *Coord. Chem. Rev.* **2020**, *408*, 213178.
(11) Alam, P.; He, W.; Leung, N. L. C.; Ma, C.; Kwok, R. T. K.; Lam, J. W. Y.; Sung, H. H. Y.; Williams, I. D.; Wong, K. S.; Tang, B. Z. Red AIE-Active Fluorescent Probes with Tunable Organelle-Specific Targeting. *Adv. Funct. Mater.* **2020**, *30* (10), 1909268.
(12) Shi, L.; Li, K.; Li, L.-L.; Chen, S.-Y.; Li, M.-Y.; Zhou, Q.; Wang, N.; Yu, X.-Q. Novel Easily Available Purine-Based AIEgens with Colour Tunability and Applications in Lipid Droplet Imaging. *Chem. Sci.* **2018**, *9* (48), 8969−8974.
(13) Collot, M.; Fam, T. K.; Ashokkumar, P.; Faklaris, O.; Galli, T.; Danglot, L.; Klymchenko, A. S. Ultrabright and Fluorogenic Probes for Multicolor Imaging and Tracking of Lipid Droplets in Cells and Tissues. *J. Am. Chem. Soc.* **2018**, *140* (16), 5401−5411.
(14) Fam, T. K.; Klymchenko, A. S.; Collot, M. Recent Advances in Fluorescent Probes for Lipid Droplets. *Materials (Basel)* **2018**, *11* (9), 1768.
(15) Zhao, N.; Li, Y.; Yang, W.; Zhuang, J.; Li, Y.; Li, N. Multifunctional Pyrazoline Based AIEgens: Real-Time Tracking and Specific Protein "Fishing" of Lipid Droplets. *Chem. Sci.* **2019**, *10* (39), 9009−9016.
(16) Zheng, X.; Zhu, W.; Ni, F.; Ai, H.; Gong, S.; Zhou, X.; Sessler, J. L.; Yang, C. Simultaneous Dual-Colour Tracking Lipid Droplets and Lysosomes Dynamics Using a Fluorescent Probe. *Chem. Sci.* **2019**, *10* (8), 2342−2348.
(17) Nagy, L. I.; Molnár, E.; Kanizsai, I.; Madácsi, R.; Ózsvári, B.; Fehér, L. Z.; Fábián, G.; Marton, A.; Vizler, C.; Ayaydin, F.; Kitajka, K.; Hackler, L.; Mátés, L.; Deák, F.; Kiss, I.; Puskás, L. G. Lipid Droplet Binding Thalidomide Analogs Activate Endoplasmic Reticulum Stress and Suppress Hepatocellular Carcinoma in a Chemically Induced Transgenic Mouse Model. *Lipids Health Dis* **2013**, *12*, 175.
(18) Foissner, I. Fluorescent Phosphocholine-a Specific Marker for the Endoplasmic Reticulum and for Lipid Droplets in Chara Internodal Cells. *Protoplasma* **2009**, *238* (1−4), 47−58.
(19) Guo, L.; Tian, M.; Zhang, Z.; Lu, Q.; Liu, Z.; Niu, G.; Yu, X. Simultaneous Two-Color Visualization of Lipid Droplets and Endoplasmic Reticulum and Their Interplay by Single Fluorescent Probes in Lambda Mode. *J. Am. Chem. Soc.* **2021**, *143* (8), 3169−3179.
(20) Kowada, T.; Maeda, H.; Kikuchi, K. BODIPY-Based Probes for the Fluorescence Imaging of Biomolecules in Living Cells. *Chem. Soc. Rev.* **2015**, *44* (14), 4953−4972.

(21) Gorai, S.; Ghosh, A.; Chakraborty, S.; Retailleau, P.; Ghanty, T. K.; Patro, B. S.; Mula, S. Fluorescent Cu2+ Sensor Based on Phenanthroline-BODIPY Conjugate: A Mechanistic Study. *Dyes Pigm.* **2022**, *203*, 110343.
(22) Pachpatil, P. K.; Kanojia, S. V.; Ghosh, A.; Majumdar, A. G.; Wadawale, A.; Mohapatra, M.; Patro, B. S.; Ghanty, T. K.; Goswami, D. Stable, Triplet Ground State BODIPY-TEMPO Diradical as a Selective Turn on Fluorescence Sensor for Intracellular Labile Iron Pool. *Sens. Actuators, B* **2022**, *370*, 132474.
(23) Chiu, C.-F.; Lai, G.-Y.; Chen, C.-H.; Chiu, C.-C.; Hung, S.-W.; Chang, C.-F. 6,7-Dihydroxy-2-(4'-Hydroxyphenyl)Naphthalene Induces HCT116 Cell Apoptosis through Activation of Endoplasmic Reticulum Stress and the Extrinsic Apoptotic Pathway. *Drug Des Devel Ther* **2019**, *13*, 1609−1621.
(24) Van Winkle, L. S.; Johnson, Z. A.; Nishio, S. J.; Brown, C. D.; Plopper, C. G. Early Events in Naphthalene-Induced Acute Clara Cell Toxicity: Comparison of Membrane Permeability and Ultrastructure. *Am. J. Respir. Cell Mol. Biol.* **1999**, *21* (1), 44−53.
(25) Ghule, N. V.; Bhosale, R. S.; Kharat, K.; Puyad, A. L.; Bhosale, S. V.; Bhosale, S. V. A Naphthalenediimide-Based Fluorescent Sensor for Detecting the PH within the Rough Endoplasmic Reticulum of Living Cells. *ChemPlusChem.* **2015**, *80* (3), 485−489.
(26) Tajima, K.; Fukui, N.; Shinokubo, H. Aggregation-Induced Emission of Nitrogen-Bridged Naphthalene Monoimide Dimers. *Org. Lett.* **2019**, *21* (23), 9516−9520.
(27) Chakraborty, D.; Sarkar, D.; Ghosh, A. K.; Das, P. K. Lipase Sensing by Naphthalene Diimide Based Fluorescent Organic Nanoparticles: A Solvent Induced Manifestation of Self-Assembly. *Soft Matter* **2021**, *17* (8), 2170−2180.
(28) Zhao, J.; Xu, K.; Yang, W.; Wang, Z.; Zhong, F. The Triplet Excited State of Bodipy: Formation, Modulation and Application, Chem. *Soc. Rev.* **2015**, *44*, 8904−8939.
(29) Kamkaew, A.; Lim, S. H.; Lee, H. B.; Kiew, L. V.; Chung, L. Y.; Burgess, K. BODIPY Dyes in Photodynamic Therapy, Chem. *Soc. Rev.* **2013**, *42*, 77−88.
(30) Zhang, X.-F.; Feng, N. Attaching Naphthalene Derivatives onto BODIPY for Generating Excited Triplet State and Singlet Oxygen: Tuning PET-Based Photosensitizer by Electron Donors. *Spectrochim. Acta A Mol. Biomol. Spectrosc.* **2018**, *189*, 13−21.
(31) Yogo, T.; Urano, Y.; Ishitsuka, Y.; Maniwa, F.; Nagano, T. Highly Efficient and Photostable Photosensitizer Based on BODIPY Chromophore. *J. Am. Chem. Soc.* **2005**, *127* (35), 12162−12163.
(32) Koli, M. R.; Labiod, A.; Chakraborty, S.; Kumar, M.; Lévêque, P.; Ulrich, G.; Leclerc, N.; Jacquemin, D.; Mula, S. Tuning the Emission Color of Indolo [3, 2-b] Carbazole-Based Boron Complexes and Their Application in Organic Field Effect Transistors and Bioimaging. *ChemPhotoChem.* **2020**, *4* (9), 729−741.
(33) Gupta, P.; Majumdar, A. G.; Patro, B. S. Non-Enzymatic Function of WRN RECQL Helicase Regulates Removal of Topoisomerase-I-DNA Covalent Complexes and Triggers NF-KB Signaling in Cancer. *Aging Cell* **2022**, *21* (6), No. e13625.
(34) Khatoon, S. S.; Chen, Y.; Zhao, H.; Lv, F.; Liu, L.; Wang, S. In Situ Self-Assembly of Conjugated Polyelectrolytes for Cancer Targeted Imaging and Photodynamic Therapy. *Biomater. Sci.* **2020**, *8* (8), 2156−2163.
(35) Wilkinson, F.; Helman, W. P.; Ross, A. B. Quantum Yields for the Photosensitized Formation of the Lowest Electronically Excited Singlet State of Molecular Oxygen in Solution. *J. Phys. Chem. Ref. Data* **1993**, *22* (1), 113−262.
(36) Karges, J.; Heinemann, F.; Jakubaszek, M.; Maschietto, F.; Subecz, C.; Dotou, M.; Vinck, R.; Blacque, O.; Tharaud, M.; Goud, B.; Viñuelas Zahı Nos, E.; Spingler, B.; Ciofini, I.; Gasser, G. Rationally Designed Long-Wavelength Absorbing Ru(II) Polypyridyl Complexes as Photosensitizers for Photodynamic Therapy. *J. Am. Chem. Soc.* **2020**, *142* (14), 6578−6587.
(37) Gupta, M.; Mula, S.; Tyagi, M.; Ghanty, T. K.; Murudkar, S.; Ray, A. K.; Chattopadhyay, S. Rational Design of Boradiazaindacene (BODIPY)-Based Functional Molecules. *Chem. Eur. J.* **2013**, *19* (52), 17766−17772.
(38) Rubbiani, R.; Wu, W.; Naik, A.; Larocca, M.; Schneider, L.; Padrutt, R.; Babu, V.; König, C.; Hinger, D.; Maake, C.; Ferrari, S.; Gasser, G.; Spingler, B. Studying the Cellular Distribution of Highly Phototoxic Platinated Metalloporphyrins Using Isotope Labelling. *Chem. Commun.* **2020**, *56* (92), 14373−14376.
(39) Mirzayans, R.; Andrais, B.; Scott, A.; Tessier, A.; Murray, D. A Sensitive Assay for the Evaluation of Cytotoxicity and Its Pharmacologic Modulation in Human Solid Tumor-Derived Cell Lines Exposed to Cancer-Therapeutic Agents. *J. Pharm. Pharm. Sci.* **2007**, *10* (2), 298s−311s.
(40) Chipurupalli, S.; Ganesan, R.; Martini, G.; Mele, L.; Reggio, A.; Esposito, M.; Kannan, E.; Namasivayam, V.; Grumati, P.; Desiderio, V.; Robinson, N. Cancer Cells Adapt FAM134B/BiP Mediated ER-Phagy to Survive Hypoxic Stress. *Cell Death Dis* **2022**, *13* (4), 1−13.
(41) Robin, M. J. D.; Appelman, M. D.; Vos, H. R.; van Es, R. M.; Paton, J. C.; Paton, A. W.; Burgering, B.; Fickert, P.; Heijmans, J.; van de Graaf, S. F. J. Calnexin Depletion by Endoplasmic Reticulum Stress During Cholestasis Inhibits the Na+-Taurocholate Cotransporting Polypeptide. *Hepatol Commun.* **2018**, *2* (12), 1550−1566.
(42) Dai, Z.; Zhang, W.; Zhou, L.; Huang, J. Probing Lipid Peroxidation in Ferroptosis: Emphasizing the Utilization of C11-BODIPY-Based Protocols. *Methods Mol. Biol.* **2023**, *2712*, 61−72.
(43) Dong, X.; Zeng, Y.; Zhang, Z.; Fu, J.; You, L.; He, Y.; Hao, Y.; Gu, Z.; Yu, Z.; Qu, C.; Yin, X.; Ni, J.; Cruz, L. J. Hypericin-Mediated Photodynamic Therapy for the Treatment of Cancer: A Review. *J. Pharm. Pharmacol* **2021**, *73* (4), 425−436.
(44) Gomes-da-Silva, L. C.; Zhao, L.; Bezu, L.; Zhou, H.; Sauvat, A.; Liu, P.; Durand, S.; Leduc, M.; Souquere, S.; Loos, F.; Mondragón, L.; Sveinbjørnsson, B.; Rekdal, Ø.; Boncompain, G.; Perez, F.; Arnaut, L. G.; Kepp, O.; Kroemer, G. Photodynamic Therapy with Redaporfin Targets the Endoplasmic Reticulum and Golgi Apparatus. *EMBO J.* **2018**, *37* (13), No. e98354.
(45) Petan, T.; Jarc, E.; Jusović, M. Lipid Droplets in Cancer: Guardians of Fat in a Stressful World. *Molecules* **2018**, *23* (8), 1941.
(46) Suwara, J.; Lukasik, B.; Zurawinski, R.; Pawlowska, R.; Chworos, A. Highly Fluorescent Distyrylnaphthalene Derivatives as a Tool for Visualization of Cellular Membranes. *Materials* **2020**, *13* (4), 951.
(47) Guardia-Laguarta, C.; Area-Gomez, E.; Schon, E. A.; Przedborski, S. Novel Subcellular Localization for α-Synuclein: Possible Functional Consequences. *Front Neuroanat* **2015**, *9*, 17.
(48) Olzmann, J. A.; Carvalho, P. Dynamics and Functions of Lipid Droplets. *Nat. Rev. Mol. Cell Biol.* **2019**, *20* (3), 137−155.
(49) den Hartigh, L. J.; Connolly-Rohrbach, J. E.; Fore, S.; Huser, T. R.; Rutledge, J. C. Fatty Acids from Very Low-Density Lipoprotein Lipolysis Products Induce Lipid Droplet Accumulation in Human Monocytes. *J. Immunol* **2010**, *184* (7), 3927−3936.
(50) Mansuri, S.; Mahalingavelar, P.; Soppina, V.; Kanvah, S. A Two-in-One Probe: Imaging Lipid Droplets and Endoplasmic Reticulum in Tandem. *J. Mater. Chem. B* **2024**, *12* (8), 2028−2041.
(51) Ghule, N. V.; La, D. D.; Bhosale, R. S.; Al Kobaisi, M.; Raynor, A. M.; Bhosale, S. V.; Bhosale, S. V. Effect of Amide Hydrogen Bonding Interaction on Supramolecular Self-Assembly of Naphthalene Diimide Amphiphiles with Aggregation Induced Emission. *ChemistryOpen* **2016**, *5* (2), 157−163.
(52) Zhou, L.; Wei, F.; Xiang, J.; Li, H.; Li, C.; Zhang, P.; Liu, C.; Gong, P.; Cai, L.; Wong, K. M.-C. Enhancing the ROS Generation Ability of a Rhodamine-Decorated Iridium(III) Complex by Ligand Regulation for Endoplasmic Reticulum-Targeted Photodynamic Therapy. *Chem. Sci.* **2020**, *11* (44), 12212−12220.
(53) Zhou, Y.; Cheung, Y.-K.; Ma, C.; Zhao, S.; Gao, D.; Lo, P.-C.; Fong, W.-P.; Wong, K. S.; Ng, D. K. P. Endoplasmic Reticulum-Localized Two-Photon-Absorbing Boron Dipyrromethenes as Advanced Photosensitizers for Photodynamic Therapy. *J. Med. Chem.* **2018**, *61* (9), 3952−3961.
(54) Li, S.; Chen, Y.; Wu, Y.; Yao, S.; Yuan, H.; Tan, Y.; Qi, F.; He, W.; Guo, Z. An Endoplasmic Reticulum Targeting Type I Photosensitizer for Effective Photodynamic Therapy against Hypoxic Tumor Cells. *Chem.Eur. J.* **2022**, *28* (72), No. e202202680.

https://doi.org/10.1021/jacsau.3c00539
JACS Au 2024, 4, 2838−2852

(55) Xiong, T.; Chen, Y.; Peng, Q.; Lu, S.; Long, S.; Li, M.; Wang, H.; Lu, S.; Chen, X.; Fan, J.; Wang, L.; Peng, X. Lipid Droplet Targeting Type I Photosensitizer for Ferroptosis via Lipid Peroxidation Accumulation. *Adv. Mater.* **2024**, *36* (4), 2309711.
(56) Karges, J.; Basu, U.; Blacque, O.; Chao, H.; Gasser, G. Polymeric Encapsulation of Novel Homoleptic Bis(Dipyrrinato) Zinc(II) Complexes with Long Lifetimes for Applications as Photodynamic Therapy Photosensitisers. *Angew. Chem., Int. Ed.* **2019**, *58* (40), 14334−14340.
(57) Rizvi, I.; Nath, S.; Obaid, G.; Ruhi, M. K.; Moore, K.; Bano, S.; Kessel, D.; Hasan, T. A Combination of Visudyne and a Lipid-Anchored Liposomal Formulation of Benzoporphyrin Derivative Enhances Photodynamic Therapy Efficacy in a 3D Model for Ovarian Cancer. *Photochem. Photobiol.* **2019**, *95* (1), 419−429.
(58) Karimnia, V.; Slack, F. J.; Celli, J. P. Photodynamic Therapy for Pancreatic Ductal Adenocarcinoma. *Cancers (Basel)* **2021**, *13* (17), 4354.
(59) Gupta, P.; Saha, B.; Chattopadhyay, S.; Patro, B. S. Pharmacological Targeting of Differential DNA Repair, Radio-Sensitizes WRN-Deficient Cancer Cells in Vitro and in Vivo. *Biochem. Pharmacol.* **2021**, *186*, 114450.
(60) Gupta, M.; Mula, S.; Ghanty, T.; Naik, D.; Ray, A.; Sharma, A.; Chattopadhyay, S. Structure and Solvent-Induced Tuning of Laser Property and Photostability of a Boradiazaindacene (BODIPY) Dye. *J. Photochem. Photobiol., A* **2017**, *349*, 162−170.
(61) Pai Bellare, G.; Sankar Patro, B. Resveratrol Sensitizes Breast Cancer to PARP Inhibitor, Talazoparib through Dual Inhibition of AKT and Autophagy Flux. *Biochem. Pharmacol.* **2022**, *199*, 115024.
(62) Chakraborty, S.; Dutta, K.; Gupta, P.; Das, A.; Das, A.; Ghosh, S. K.; Patro, B. S. Targeting RECQL5 Functions, by a Small Molecule, Selectively Kills Breast Cancer in Vitro and in Vivo. *J. Med. Chem.* **2021**, *64* (3), 1524−1544.
(63) Guha Majumdar, A.; Shree, S.; Das, A.; Kumar, B. K.; Dey, P.; Subramanian, M.; Patro, B. S. Design, Synthesis and Development of a Dual Inhibitor of Topoisomerase 1 and Poly (ADP-Ribose) Polymerase 1 for Efficient Killing of Cancer Cells. *Eur. J. Med. Chem.* **2023**, *258*, 115598.
(64) Tyagi, M.; Bauri, A. K.; Chattopadhyay, S.; Patro, B. S. Thiol Antioxidants Sensitize Malabaricone C Induced Cancer Cell Death via Reprogramming Redox Sensitive P53 and NF-KB Proteins in Vitro and in Vivo. *Free Radic Biol. Med.* **2020**, *148*, 182−199.
(65) Becke, A. D. A New Mixing of Hartree-Fock and Local Density-functional Theories. *J. Chem. Phys.* **1993**, *98* (2), 1372−1377.
(66) Lee, C.; Yang, W.; Parr, R. G. Development of the Colle-Salvetti Correlation-Energy Formula into a Functional of the Electron Density. *Phys. Rev. B* **1988**, *37* (2), 785−789.
(67) Schmidt, M. W.; Baldridge, K. K.; Boatz, J. A.; Elbert, S. T.; Gordon, M. S.; Jensen, J. H.; Koseki, S.; Matsunaga, N.; Nguyen, K. A.; Su, S.; Windus, T. L.; Dupuis, M.; Montgomery, J. A., Jr General Atomic and Molecular Electronic Structure System. *J. Comput. Chem.* **1993**, *14* (11), 1347−1363.
(68) Weigend, F.; Ahlrichs, R. Balanced Basis Sets of Split Valence, Triple Zeta Valence and Quadruple Zeta Valence Quality for H to Rn: Design and Assessment of Accuracy. *Phys. Chem. Chem. Phys.* **2005**, *7* (18), 3297−3305.

https://doi.org/10.1021/jacsau.3c00539
JACS Au 2024, 4, 2838−2852